Feature Article:

The Lunar Polar Hydrogen Mapper CubeSat Mission

Craig Hardgrove, **ASU School of Earth and Space Exploration**
Richard Starr, **NASA/Goddard Space Flight Center**
Igor Lazbin, **AZ Space Technologies**
Alessandra Babuscia, **Jet Propulsion Laboratory**
Bob Roebuck, **AZ Space Technologies**
Joe DuBois, **ASU School of Earth and Space Exploration**
Nathaniel Struebel, **AZ Space Technologies**
Anthony Colaprete, **NASA Ames Research Center**
Darrell Drake, **TechSource LLC**
Erik Johnson, James Christian, **Radiation Monitoring Devices**
Lena Heffern, **ASU School of Earth and Space Exploration**
Steve Stem, **Blue Canyon Technologies, LLC**
Sean Parlapiano, Mitchel Wiens, **MMA Design LLC**
Anthony Genova, **NASA Ames Research Center**
David Dunham, Derek Nelson, Bobby Williams, Jeremy Bauman, **KinetX Aerospace**
Patrick Hailey, Tyler O'Brien, **Qwaltec, Inc.**
Kabir Marwah, Logan Vlieger, James Bell, **ASU School of Earth and Space Exploration**
Tom Prettyman, **Planetary Science Institute**
Teri Crain, Ernest Cisneros, Nathan Cluff, **School of Earth and Space Exploration, Arizona State University**
*Graham Stoddard, Meghan Kaffine,* **Radiation Monitoring Devices**

Authors' current addresses: Craig Hardgrove, Joe DuBois, Lena Heffern, Kabir Marwah, Logan Vlieger, James Bell, ASU School of Earth and Space Exploration, PO Box 876004, Tempe, AZ 85287-6004, USA. (e-mails: craig.hardgrove@asu.edu, joe.dubois@asu.edu, lheffern@asu.edu, kabir.marwah15@imperial.ac.uk, Jim.Bell@asu.edu). Richard Starr, NASA/Goddard Space Flight Center, Code 691, Greenbelt, MD 20771, USA. (e-mail: richard.d.starr@nasa.gov). Igor Lazbin, Bob Roebuck, Nathaniel Struebel, 70 S. Val Vista Dr, A3-191, Gilbert, AZ 85296, USA. (e-mails: Igor.lazbin@azspacetech.com, bob.roebuck@azspacetech.com, nathaniel.struebel@azspacetech.com). Alessandra Babuscia, 4800 Oak Grove Dr., Pasadena, CA 91109, USA. (e-mail: Alessandra.Babuscia@jpl.nasa.gov). Anthony Colaprete, NASA Ames Research Center, Moffett Field, MS 245-3, Mountain View, CA 94035, USA. (e-mail: anthony.colaprete-1@nasa.gov). Darrell Drake, 221 La Cruz Rd, Santa Fe, NM 87501, USA. (e-mail: chezdrake@gmail.com). Erik Johnson, 44 Hunt Street, Watertown, MA 02472, USA. (e-mail: ejohnson@rmdinc.com). James Christian, 44 Hunt St., Watertown, MA 02472, USA. (e-mail: JChristian@RMDinc.com). Steve Stem, Blue Canyon Technologies, LLC, 5330 Airport Blvd, Suite 100, Boulder, CO 80301, USA. (e-mail: sstem@bluecanyontech.com). Sean Parlapiano, Mitchel Wiens, MMA Design LLC, 2000 Taylor Avenue, Suite 200, Louisville, CO 80027, USA. (e-mails: sparlapiano@mmadesignllc.com, mwiens@mmadesignllc.com). Anthony Genova, NASA Ames Research Center, MS 202-1, Moffett Field, CA 94035, USA. (e-mail: Anthony.Genova@nasa.gov). David Dunham, Bobby Williams, Jeremy Bauman, 2050 East ASU Circle, Suite 107, Tempe, AZ 85284-1839, USA. (e-mails: david.dunham@kinetx.com, bobby.williams@kinetx.com, jbauman@kinetx.com). Patrick Hailey, Tyler O'Brien, 8950 S. 52nd St, Suite 409, Tempe, AZ 85284, USA. (e-mails: phailey@qwaltec.com, tobrien@qwaltec.com). Tom Prettyman, 6509 Caballero Pkwy NW, Los Ranchos de Albuquerque, NM 87107, USA. (e-mail: prettyman@psi.edu). Teri Crain, Ernest Cisneros, Nathan Cluff, School of Earth and Space Exploration, Arizona State University, PO Box 876004, Tempe, AZ 85287-6004, USA. (e-mails: Teri.Crain@asu.edu, ecisneros@asu.edu, nacluff@asu.edu). Graham Stoddard, Meghan Kaffine, Radiation Monitoring Devices, 44 Hunt Street, Watertown, MA 02472, USA. (e-mails: gstoddard@rmdinc.com, mkaffine@rmdinc.com)
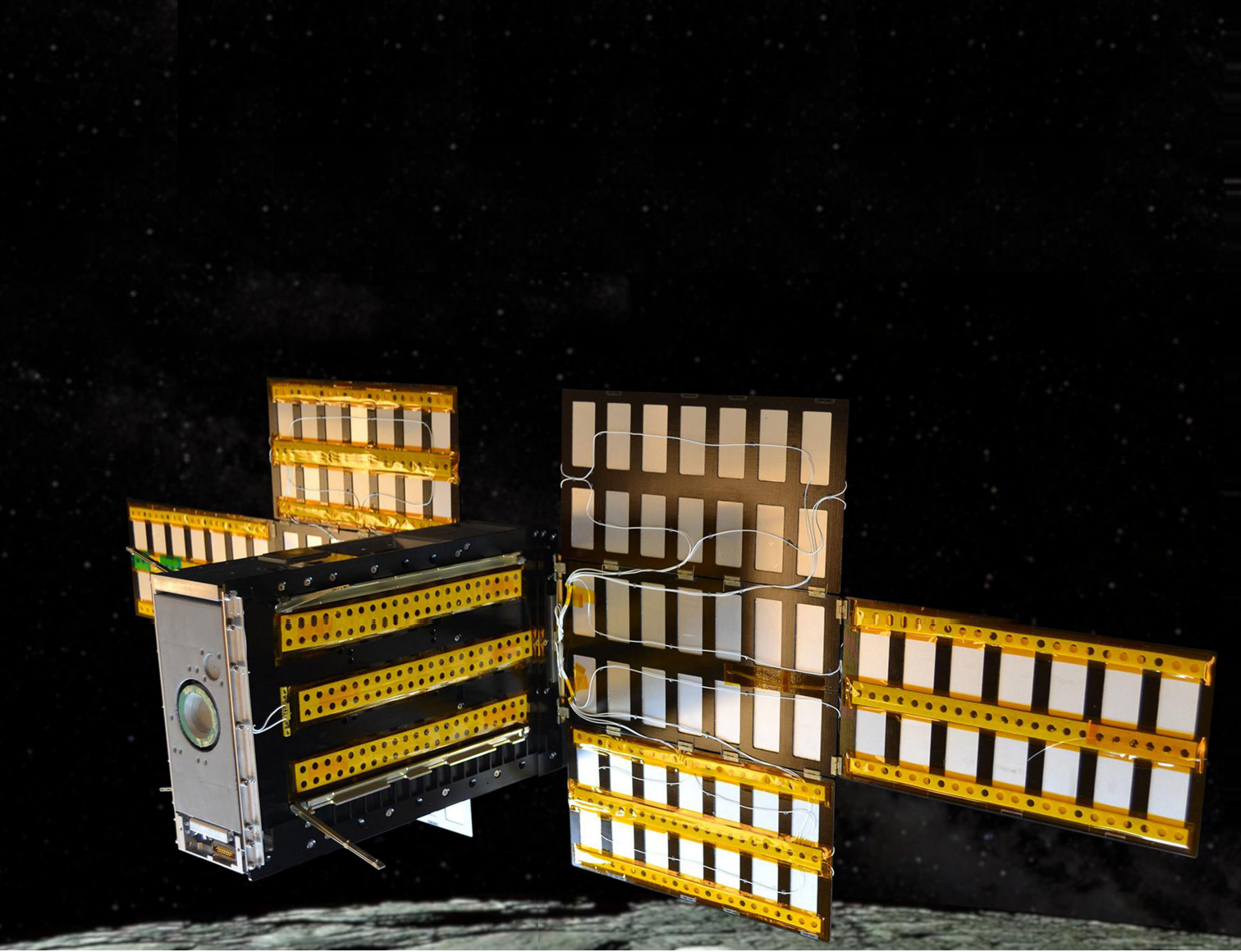
INTRODUCTION

OVER the last several decades, observations of polar regions on airless planetary bodies have revealed water-ice enrichments located within and around permanently shadowed regions (PSRs) [12], [21], [25]. At the lunar South Pole, these observations could be accounted for by significant amounts of water ice concentrated within relatively small patches [10]. The distribution and magnitude of these enrichments, however, is not uniform from one PSR to the next and is poorly constrained at spatial scales of less than several tens of kilometers [14], [18], [37]. These nonuniformities are not well understood and suggest that we still do not fully understand the origin, nature, and distribution of the bulk lunar polar volatile inventory. The changing paleopole position of the Moon could account for aspects of the observed asymmetrical distribution of bulk hydrogen at both poles, however, current datasets do not resolve the polar PSRs completely, making the nature of the observed asymmetrical distribution of polar hydrogen uncertain [35]. Measurements of

the bulk hydrogen content of lunar regolith at the lunar poles that are at spatial scales small enough to resolve the PSRs will inform models of ice emplacement and preservation and could identify regions at the lunar South Pole that are not in permanent shadow but where ancient ice may be preserved [34]. In addition, the lunar polar volatile inventory appears to be much lower than the volatile inventory observed on Mercury. PSRs at Mercury's poles contain nearly an order of magnitude greater amounts of hydrated material, likely water ice, which appear in patchy and nonuniform distributions [23]. Placing meaningful constraints on the bulk abundance and distribution of hydrated materials within PSRs of the Moon will help constrain models of volatile delivery to the inner solar system. In addition, an improved understanding of the small-scale (~tens of km) water-ice enrichments at the lunar poles has implications for future human lunar exploration, as water ice is an extremely valuable resource. The lunar South Pole is ideal for this study, as the PSRs have been extensively studied and are spatially larger in the South Pole than the lunar North

Pole, making them easier to spatially resolve with neutron spectroscopy [34].

Previous NASA planetary science missions to the Moon have used neutron spectroscopy from orbit to map bulk hydrogen distributions across the lunar surface. Neutron spectrometers detect the neutrons created within planetary surfaces by interactions with galactic cosmic rays (GCR) that interact with regolith and subsequently escape the planetary surface. The energy distribution of escaping neutrons is a function of the bulk chemistry, hydrogen abundance, depth distribution of hydrogen, and a variety of other factors related to the regolith and surface properties ([30]; [20], [32]; [11]; [33]). Neutrons in the energy range of $\sim$0.4 eV to $\sim$10 keV will be most sensitive to hydrogen abundance and have been used to map quantities of hydrogen down to $\sim$50 ppm [22]. From orbit, however, neutron detectors typically have a poor spatial resolution, with an effective field of view of about one and a half times the orbital altitude [20]. Previous lunar spacecraft have orbited at altitudes of tens to hundreds of kilometers, resulting in coarse (many kilometer-scale) maps of neutron counts [12], [25]. These maps are sufficient to reveal the regional hydrogen distribution at the poles but are not high enough resolution to determine the distribution of hydrogen within permanently shadowed craters. A low cost, high risk balanced by high payoff CubeSat mission to the Moon represents one possible path to providing higher spatial resolution neutron maps of these regions that may be enriched in water ice at the Moon.

The Lunar Polar Hydrogen Mapper (LunaH-Map) mission, selected by NASA's Science Mission Directorate in late-2015 as part of the Small Innovative Missions for PLanetary Science program, will help identify regions of hydrogen enrichment at the lunar South Pole and place important constraints on the distribution of lunar polar volatiles within PSRs. The LunaH-Map spacecraft is designed to fit within a 6U+ CubeSat form factor carrying one science instrument, a new type of neutron spectrometer. A new type of detector material is used, as this was required to achieve sufficient efficiencies for neutron detection in such a small volume. In order to improve upon the spatial resolution achieved by previous neutron instruments at the Moon, LunaH-Map will achieve perilune altitudes between 10 and 15 km above the lunar surface. The resulting mission profile is unlike anything that would be considered, at least during the nominal science phase, in a much larger NASA interplanetary spacecraft mission.

The goals of the LunaH-Map mission are to acquire scientific data about hydrogen distributions at the lunar poles using a calibrated planetary science instrument on board a new, highly specialized, spacecraft platform. LunaH-Map will also demonstrate a high-risk mission profile and trajectory design that would only be considered within this new paradigm of small, rapid, repeatable, interplanetary science-driven CubeSat missions. At the time of the writing of this article, the launch date and trajectory of the launch vehicle for LunaH-Map is uncertain, which will influence the trans-lunar orbit maneuvers as well as navigation and operations requirements. In addition, the flight spacecraft has begun integration and testing but is not yet in the final configuration. Thus, the final design details, implementation (including instrument calibration and testing) and operations plan will be presented after the spacecraft has been delivered to the launch vehicle. Herein, we provide an overview and description of the science, mission design, instrumentation, and development of several subsystems on the LunaH-Map spacecraft.

SCIENCE

Understanding the nature and distribution of water and other volatiles at the Moon and in other solar system bodies has been a subject of intense interest for planetary science [24]. Urey [40] and Watson, Murray and Brown [41] were among the first to suggest that PSRs at the lunar poles might contain water ice. Arnold [1] revisited the issue of long-term stability of water ice and other volatiles sequestered within lunar PSRs and determined that lifetimes of order 2–3 billion years were possible. The Bistatic Radar Experiment on the Clementine spacecraft provided the first observational support for this idea [28]. The detection of reduced epithermal neutron flux at the poles by neutron experiments on board the Lunar Prospector (LP) spacecraft and the Lunar Reconnaissance Orbiter (LRO) provided positive identification of increased hydrogen concentrations at the poles, possibly in the form of water ice around PSRs [12], [25]. Further evidence was obtained by the Lunar Crater Observation and Sensing Satellite that detected water vapor in the ejecta plume from the impact of its spent Centaur rocket into the Cabeus crater near the lunar South Pole [5]. The relatively coarse spatial resolution of the previous orbital neutron measurements made from LP and LRO cannot confirm that bulk hydrogen enrichments are positively correlated with PSRs, as a portion of the neutron signal corresponds to the illuminated (or partially illuminated) portions of the lunar South Pole. Alternatively, orbital neutron measurements made by LP and LRO from outside but near PSRs may contain contributions to the neutron signal from within the PSRs themselves. It is possible, therefore, that the observations made by LP and LRO are consistent with ancient buried ice at the lunar South Pole concentrated in some regions of partial or full illumination. By making low altitude passes over the lunar South Pole with a neutron spectrometer,
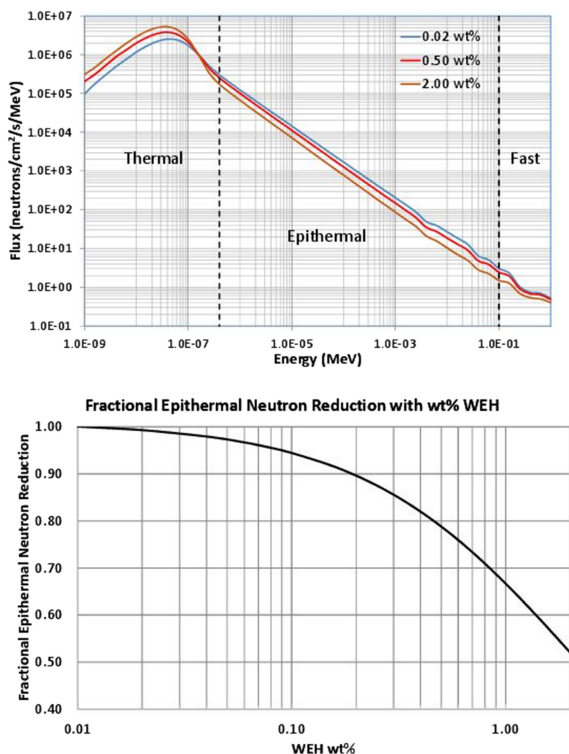
Figure 1.

Top plot shows simulated lunar neutron energy spectra varying with weight percent of water-equivalent-hydrogen (WEH). The bottom plot shows the fractional reduction in epithermal neutron counts with WEH wt%.

LunaH-Map will directly observe the epithermal neutron contributions from within and outside PSRs. These epithermal neutron maps will contribute to our understanding of the geologic evolution of volatiles on the Moon and can inform future landed missions to the lunar South Pole that are focused on finding volatiles for resources. Understanding the bulk, small-scale hydrogen abundances on the Moon has the potential to reveal the nature of PSRs elsewhere in the Solar System, as similarly shadowed regions on Mercury have been observed to contain substantially more volatile than those on the Moon [21].

The source of hydrogen near the lunar surface is not well understood, although several methods for its production and redistribution to the poles have been proposed [6], [7]. Hydroxyl and H_2O can be implanted onto airless planetary surfaces by the solar wind, and these H-bearing phases can then migrate toward the poles by impacts or other processes, becoming trapped in regions of permanent shadow near the lunar poles [24]. The Moon Mineralogy Mapper (M^3) on the Indian spacecraft Chandrayaan-1 [29], the Visible and Infrared Mapping Spectrometer (VIMS) on Cassini [4] and the High Resolution Instrument–Infrared spectrometer on Deep Impact [36] have all reported evidence for the presence of OH/H_2O in mid-latitude regions on the

Moon based on the presence of a 3.0 μm absorption feature. While these observations clearly demonstrate that the Moon is not as dry as we once thought, the source of this water is still open to debate. Implantation of solar wind H and impacts by comets and water-rich asteroids may have played a role at various times throughout the geologic history of the Moon [24].

Neutron spectroscopy is a powerful tool and has become a standard in planetary science because the energy distributions of thermal (<0.4 eV) and epithermal neutrons ($0.4–10^5$ eV) that reach the detector are highly dependent upon the hydrogen content of the top meter of a planetary surface (Figure 1). LP was the first planetary mission to carry a neutron spectrometer, but many have followed, including Mars Odyssey, the MErcury Surface, Space ENvironment, GEochemistry, and Ranging mission, LRO, the Dawn mission to Vesta and Ceres and the Dynamic Albedo of Neutrons instrument on the Mars Curiosity Rover ([9], [13]; Boynton *et al.*, 2004; [17], [26], [27], [31]). The LunaH-Map Miniature Neutron Spectrometer (Mini-NS) is the first planetary mission to use CLYC (Cs^2LiYCl^6:Ce), an inorganic scintillator with elpasolite crystal structure for neutron detection [16]. The CLYC detectors are packaged into an array making up a relatively large surface area (200 cm^2). The high efficiency of CLYC for epithermal neutrons, coupled with the low-spacecraft periapse at the Moon's South Pole will enable LunaH-Map to create maps of hydrogen within ~5 degrees of the pole that include contributions from within the lunar South Pole PSRs. Figure 1 shows the strong sensitivity of epithermal neutrons to hydrogen content. The primary science goal of the LunaH-Map mission is to evaluate the uniformity of hydrogen across the lunar South Pole. The Mini-NS has been designed with enough sensitivity to map hydrogen with good statistical confidence (~20% relative) at levels as low as 0.6% WEH (~600 μg/g H) at spatial scales $\leq$15 km^2. Preliminary analyses based on the LunaH-Map science orbit demonstrate the contribution of PSRs to the epithermal neutron signal from a set of low-altitude passes over the lunar South Pole. For a set of five orbit tracks, Figure 2 shows a preliminary assessment of the contributions from PSRs (red) to the observed epithermal neutron count rate. For the small (~kilometer) PSR labeled, the contribution of the PSR to the neutron count rate reaches ~60%.

MISSION OVERVIEW

The LunaH-Map spacecraft is equipped with a low-thrust ion propulsion system, gimbaled solar arrays, three reaction wheels, a star tracker, an X-Band radio, a command and data handling system, a power control system, and a miniature neutron spectrometer (Duncan C., 2015, Cheung, K.M., 2015). After deployment, LunaH-Map will
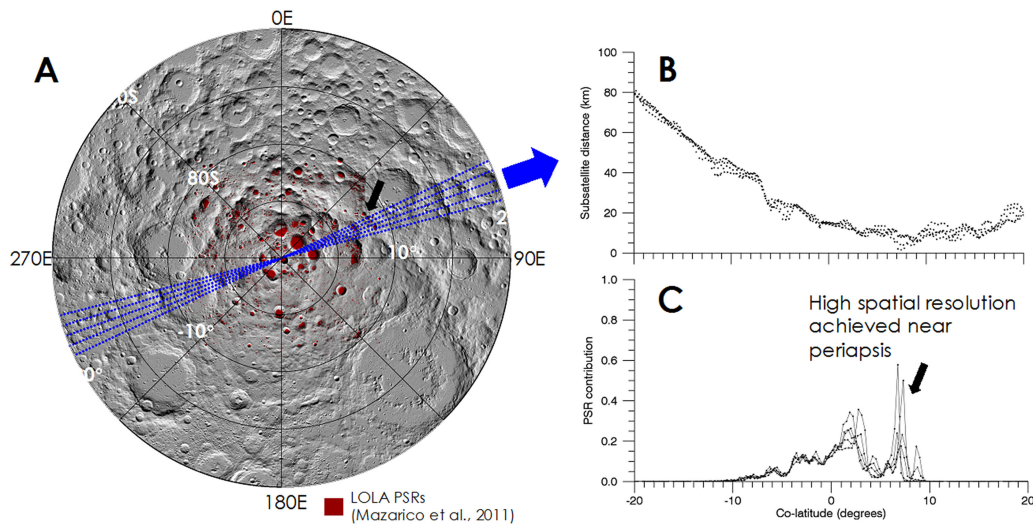
Figure 2.
A) Subset of five science orbit tracks (blue dotted lines) with PSRs shown in red. Data are superimposed on Moon LRO LOLA Hillshade 237m v4, LOLA Science Team, retrieved from USGS web site. B) Subsatellite distance above terrain vs co-latitude for the five science orbits shown in A. C) Contribution from PSRs to the epithermal neutron count rate along the five science orbits shown. The black arrow in C and A highlights the small (∼kilometer wide) PSR for which the epithermal neutron contribution reaches 50%–60% across several orbits.

maneuver to perform a lunar flyby targeting L2 and will eventually be captured by the Moon within two months [15]. Upon lunar capture, the spacecraft will spiral down to an elliptical low-altitude science orbit with perilune at the lunar South Pole. During the science phase, the neutron spectrometer will measure epithermal neutron counts about the perilune of each orbit when the altitude is low enough (below about 20 km) to resolve the interior of PSRs, such that their hydrogen content can be determined. Full mission success is achieved by mapping the hydrogen abundance of the lunar South Pole (poleward of 85 degrees latitude) at weight fractions of ∼600 μg/gH at a spatial scales of less than or equal to 15 km^2. Baseline mission success is achieved through verification that the neutron spectrometer (Instrument: Miniature Neutron Spectrometer section) performs successfully in cis-lunar space by detecting the signature of lunar epithermal neutrons for 30 mins (3 cps; ∼1% uncertainty). Threshold success will be achieved by verification that the Mini-NS instrument performs successfully in the space environment by measuring the expected background neutron counts in the space environment.

Systems engineering, structure, thermal, electrical harnessing, integration, test and mission operations are conducted at Arizona State University (ASU) by team members from ASU, Arizona Space Technologies and Qwaltec. Subsystem components are supplied by Radiation Monitoring Devices, Busek, Blue Canyon Technologies, JPL and MMA Designs. Navigation is supported by KinetX and NASA Ames Research Center (ARC). Catholic University, Planetary Science Institute, NASA ARC, and ASU comprise members of the science team.

TRAJECTORY DESIGN

An innovative trajectory and mission profile has been designed in order to safely deliver the LunaH-Map spacecraft into a final lunar orbit that will fulfill the mission objectives. The trajectory is partitioned into three primary phases; an Earth-Moon transfer phase, lunar orbit transition phase, and science phase, each of which presents unique challenges.

The Earth–Moon transfer phase begins with the spacecraft's deployment from the NASA Space Launch System (SLS) Artemis-1 Interim Cryogenic Propulsion Stage (ICPS) host vehicle at a distance from Earth of ∼70 000 km. This insertion state was favorable as it occurs after the ICPS has exited the Van Allen Radiation Belts, but early enough to allow time for telemetry, tracking, and propulsive maneuvers prior to the first lunar flyby, referred to as Periselene-1. Occurring 5.5 days after ICPS deployment at an altitude ∼2900 km, Periselene-1 is exercised to contain the spacecraft within the Earth–Moon system and target the Sun–Earth weak stability boundary that allows for a low-energy transfer from Periselene-1 to Lunar orbit insertion. This nominal transfer trajectory include one loop around the Earth with perigee >100 000 km altitude to avoid the Van Allen Belts and concludes with a set of maneuvers to target weak capture and orbit insertion at the second lunar encounter and orbit insertion, Periselene-2. An overview of the transfer trajectory is provided in Figure 3.

After weak capture, the lunar orbit transition phase begins with a set of maneuvers that ensures the spacecraft is captured in a stable lunar orbit. After a more stable orbit is achieved, a long cadence of maneuvers spanning several
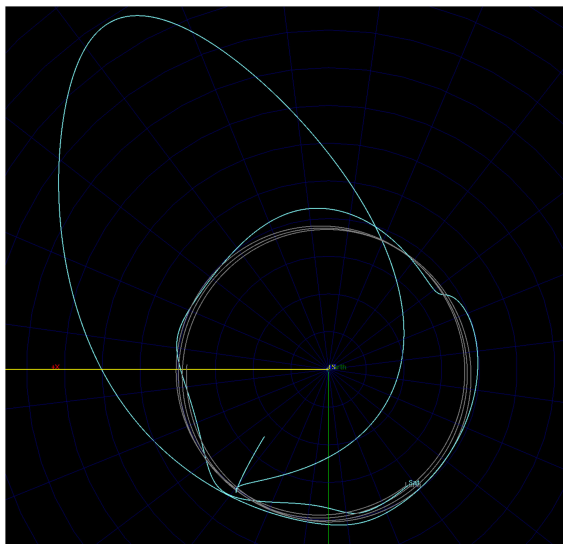
Figure 3.
LunaH-Map Transfer Trajectory. The spacecraft trajectory (cyan) leverages the first lunar swingby to enter a weak capture around Earth (origin and center of frame) and target lunar orbit insertion. The Moon's trajectory during this time span is presented in grey.

Figure 5.
LunaH-Map Science Phase. A moon-centered view of the highly elliptical (10 km × 3150 km altitude) science orbits with perilune over the Lunar South Pole. The cyan and green simply represent different halves of the orbit, and the white represents when science observations are planned to occur.

months is executed to reduce the orbital energy and eventually enter into the final science orbit. These maneuvers will occur contiguously when the spacecraft is not in eclipse or communicating with ground stations, and burn updates will occur at regular intervals to ensure the transition profile is maintained. If necessary, the spacecraft may enter a stable circular orbit during its transition to avoid Earth eclipses before targeting the final science orbit.
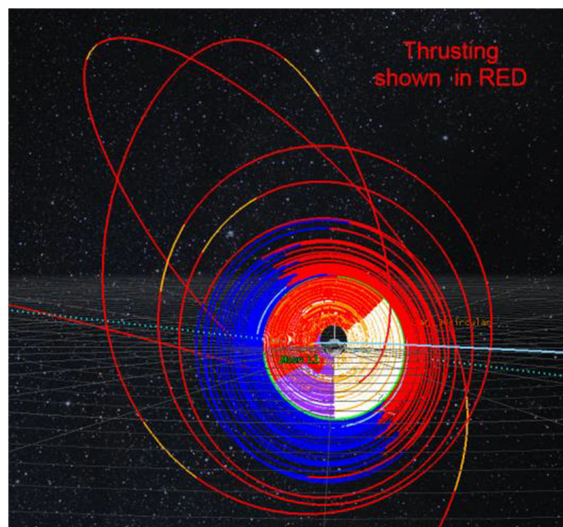

Figure 4.
LunaH-Map Transition Phase. Earth-centered view of LunaH-Map transition from weak lunar capture to elliptical science orbit. Low-thrust maneuver segments are presented in red, and all other colors are coast segments where maneuvering does not occur. The final (smallest) lunar orbit in this figure represents the 10 km × 3150 km altitude Science Orbit, also presented in Figure 5.

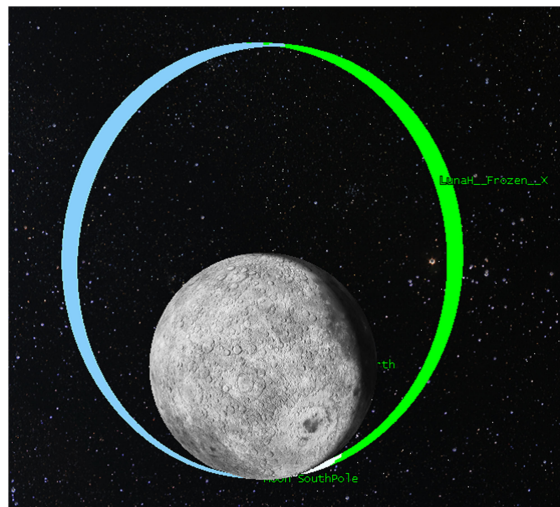After maneuvering for several months, the spacecraft's orbital parameters will match those of the final desired science orbit. An illustrated view of the transition from weak lunar capture to elliptical science orbit is shown in Figure 4.

An elliptical science orbit with periselene above the lunar South Pole will then be maintained with orbit adjustment maneuvers occurring at apolune. The periselene altitude of each pass above the South Pole will be between 5 and 25 km, enabling productive scientific return. This science orbit will be maintained for at least 282 lunar orbits (46 days), with the possibility of extending the operations and orbital maintenance if desired. The elliptical science orbit is illustrated in Figure 5.

Due to the uncertainty in the initial deployment time and state, various analyses have been conducted to analyze trajectory and orbit designs to various geometric conditions. For each different deployment state, either a one-loop (nominal) or two-loop transfer around the Earth can be found and used to target a lunar orbit insertion. The transition and science orbit's right ascension of the ascending node orbital parameter is dependent on initial deployment condition and causes different natural evolution of the other orbital parameters, none of which, however, change drastically enough to pose a threat to the nominal maneuver and operations cadence or warrant a constraint on the trajectory. However, in the event that contingency scenarios prevent navigation operations from executing the baseline trajectory, there are many possible recovery
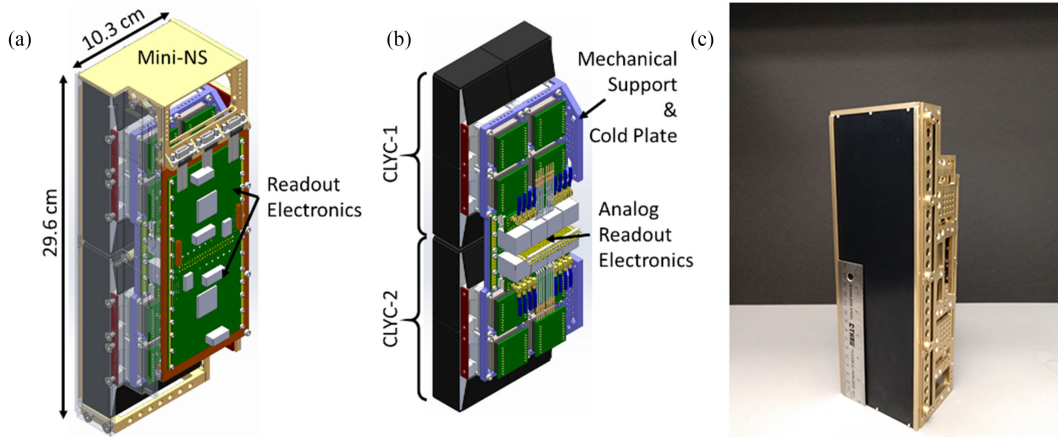
Figure 6.
a) Mechanical structure of the Mini-NS. The near-side panel is drawn as transparent to see into the instrument. b) Outer mechanics are removed showing the eight detector modules and inner readout electronics. c) Flight Mini-NS with ruler for scale.

scenarios that include rapid trajectory reoptimization and maneuver command uplinks to retarget flyby or orbital parameters.

INSTRUMENT: MINIATURE NEUTRON SPECTROMETER

OVERVIEW

The Mini-NS is located on the nadir face of the LunaH-Map spacecraft. The Mini-NS uses a set of CLYC scintillators to detect neutrons and has a gadolinium shield to provide sensitivity primarily to neutrons above 0.5 eV. The Mini-NS (Figure 6) consists of two detectors that are comprised four modules (or sensors). The modules consist of a hermetically sealed CLYC scintillator in an aluminum can, and the design provides 200 cm^2 of the scintillator's area facing the Moon. The sensors are encased with a 0.5 mm layer of gadolinium. The readout electronics are separated into two sections, where the analog components are placed near the detector and the digital electronics are further away. The digital readout electronics are mounted to the exterior support frame of the instrument, where the heat generated in these electronics is directly dissipated to the spacecraft chassis. The instrument interfaces with the spacecraft via RS422, providing a once-per-second heartbeat to monitor the instrument health. Data products are stored locally on the instrument and are time-tagged for correlation to spacecraft ephemeris. The mass of the instrument is 3.4 kg with an estimated power draw of 9.6 W. In stand-by mode, the spacecraft will interface with the instrument to transfer data or to initiate data acquisition, where the power draw in this state is estimated to be 3.6 W. The flight Mini-NS was delivered to ASU in November of 2018 and calibration data were acquired at the Los Alamos National Laboratory Neutron

Free In-Air Facility in December of 2018. The calibration data will be used to more accurately determine the detector efficiency and the energy-angle response of the two detector arrays. The details of the instrument calibration will be published in a future manuscript.

CLYC MODULES

Lunar epithermal neutrons are detected using two 2 × 2 arrays of CLYC crystals. The crystal pitch along the long axis is 68.7 mm within a set of the four modules (one detector). There is an additional gap of 4.51 mm in pitch between the modules from the detector to detector. Each CLYC module, 4 cm × 6.3 cm × 2 cm, is built to hermetically seal the crystal. The module is designed to provide space for the crystal to thermally expand and contract while maintaining a good optical connection to the quartz window. A picture of a packaged crystal is shown in Figure 7. A photomultiplier tube (PMT) is placed and sealed to the module at the window. The PMT is placed over to one corner of the module, which is an atypical design. The configuration accommodates the spatial constraints of the cubesat to provide a maximum surface area facing the Moon for a 2-cm thick crystal. The energy resolution of the gamma-ray spectroscopy is sacrificed for neutron sensitivity using this design.

The ^{6}Li (n,α) t reaction, which has a Q value of 4.8 MeV, is the dominate reaction to stop the neutrons in the crystal. The α and triton generate a light flash in the CLYC crystal that has a unique transient response compared to gamma pulses [16]. The detection efficiency for this process in CLYC maximizes at 80% for thermal neutrons. Other reaction processes capture the remaining 20%, such as the ^{35}Cl(n,p)^{35}S with a Q value of 0.6 MeV. The protons from this process are very similar to the α and triton

Figure 7.
Photograph of the packaged crystal module. The open quartz window shows the inside of the package and is the spot where the PMT will optically coupled to the module.

Figure 8.
Plot of the PSD ratio versus the energy deposited in equivalent electrons (gamma ray) energy.

particles, but the energy deposition is smaller due to the smaller Q value.

The transient information from the light flash is captured by the readout electronics, and a pulse shape discrimination (PSD) metric is used to determine if a particle is a gamma ray or a neutron. The PSD metric is a ratio of a short integral that captures the light yield from fast decay processes (<200 ns) over a longer integral that captures the yield from moderate decay processes (<1 μs). As the longer integral scales with the energy deposited (full integral 0 to 6 μs), the ratio of the short to long integrals highlights the contribution of the fast decay processes that produce light in the crystal, particularly when plotted as the PSD ratio versus the energy deposited (Figure 8). The associated energy states in the crystals to these faster decay processes are populated more readily for gamma rays compared to neutron capture events. The energy calibrated PSD analysis shows a primary neutron peak around 3 MeV, which is associated with the ^{6}Li reaction and results in particles with a kinetic energy no less than 4.8 MeV. Events below this peak cannot be caused by the ^{6}Li reaction, as they deposit less energy. These are taken as ^{35}Cl reactions, where the protons produce a light flash similar to the triton and alpha particles from the ^{6}Li reaction. Above the neutron peak, higher energy neutrons impart their energy into the triton and α particles indicating more energy deposition. Based on the kinematics of these reactions, epithermal neutrons are within the dominate neutron peak around 3 MeV in equivalent electron energy. The background signals from GCR will be primarily above this equivalent electron energy, and these high-energy protons will produce a signal similar to gamma rays. The data captured within this region (events "Gamma Rays" in Figure 7 that lie above and to the right of the events labeled "Neutrons") provides a measure of the GCR flux.
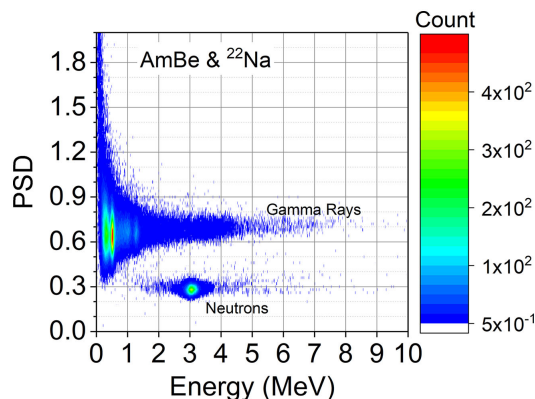
In the early phases of development [19], the crystals were packaged and thermally cycled to characterize the response of the CLYC crystals to the expected thermal environment. Thermal gradients over the crystals could be significant due to its high thermal capacity (0.4 J/g/K) and low conduction (0.007 W/cm/K at 50 C). Since the gradient is dependent on mass, geometry, and thermal rates, testing has been conducted to establish the nominal instrument operational conditions. We imposed a rate of 0.5 C/min, which is within the anticipated rate from thermal modules during flight. Further measures to prevent light loss from crystal degradation due to thermal cycling include using a thicker optical gel pad and a softer foam backing in the Mini-NS module design.

READOUT ELECTRONICS

The signals from the PMTs are summed to a single analog to digital converter operated at 250 mega-samples per second. The digitized waveform from the detector is captured by an FPGA (Xilinx Zynq XQ7Z020). In addition to the summed digitized waveform, the voltage drop from the last dynode stage on the PMT is sent into a trigger to generate a logic pulse (module hit identifier). The logic pulse is used to identify which PMT generated the digitized waveform. The FPGA logic will generate another trigger to start the integration of the waveform. The algorithm in the FPGA will generate four integrals: baseline integral, short integral, long integral, and full integral. Each of the last three integrals is corrected using the baseline integral. The short and long integrals are used to generate the PSD Ratio and the full integral is used to generate the energy deposition.

A local time and set of temperatures (module and boards) are captured in the FPGA (using a counter 26-bit resolution with ~200 μs accuracy). The event-by-event data product is the most comprehensive product generated on the instrument, consisting of an event number, module

hit identifier, total number of events, energy (10-bit resolution), PSD (6-bit resolution), and local time. The event-by-event data provides a comprehensive data product to be reduced at a latter point, yet the total expected data volume may be too high to downlink due to the relatively short mission duration and limited communications availability. To provide a smaller data product that has a high probability for transmission to Earth, a reduced data set consisting of the neutron count rate is generated along with diagnostic data that will be used to assess the PSD and instrument performance. Each detector is read out separately, and the total size for each product is 6 MB (12 MB for the entire instrument) for the duration of the science phase.

SPACECRAFT

TELECOMMUNICATION

The telecommunication system for LunaH-Map is based on previously developed JPL hardware for other interplanetary CubeSat missions such as INSPIRE (Duncan 2015) and MarCO (Cheung, K.M. *et al.*, 2015). The key component of the telecommunication system is the Iris radio that provides support for telemetry, command, and navigation functions. It operates at the Near-Earth X-Band frequency range (7145–7190 MHz for uplink, 8450–8500 MHz for downlink) and provides coherent transmission with an 880/749 turn around ratio to support ranging. Uplink modulation is PCM/PSK/PM, NRZ with BCH encoding and data rates ranging from 62.5 bps to 8 Kbps. Specifically, LunaH-Map selected uplink data rates are 62.5 bps (safe mode) and 1 Kbps (nominal mode). Downlink modulation is BPSK with options for RS (255,223), convolutional ($K = 7$, $r = 1/2$) or turbo encoding (1/2,1/3,1/6 with 1784 or 8920 bit frames) and data rates ranging from 62.5 to 256 Kb/s. LunaH-Map will use 62.5 bps (safe mode) and a set of nominal mode data rates ranging from 1 to 128 Kbps. The choice of downlink data rates will depend on the phase of the mission (deployment vs. cruise, vs. science phase), the ground station used (either the 34 m dish at DSN, or the 21 m dish at Morehead State University), and the specific pointing capabilities of the spacecraft during the different mission phases. The encoding solutions implemented will mostly be alternating between Turbo 1/2 and Turbo 1/6, depending again on the mission phase and ground station used.

The Iris radio is connected in the receiving path to the Low Noise Amplifier (LNA), and the LNA is then connected to two 6 dBi patch antennas placed on the opposite side of the spacecraft for coverage maximization. In the transmitting path, the Iris radio is connected to the Solid State Power Amplifier that provides 2 W of amplification. The 2-W radio frequency signal is then transmitted through the other two 6-dBi patch antennas that are placed also on opposite sides of the spacecraft.
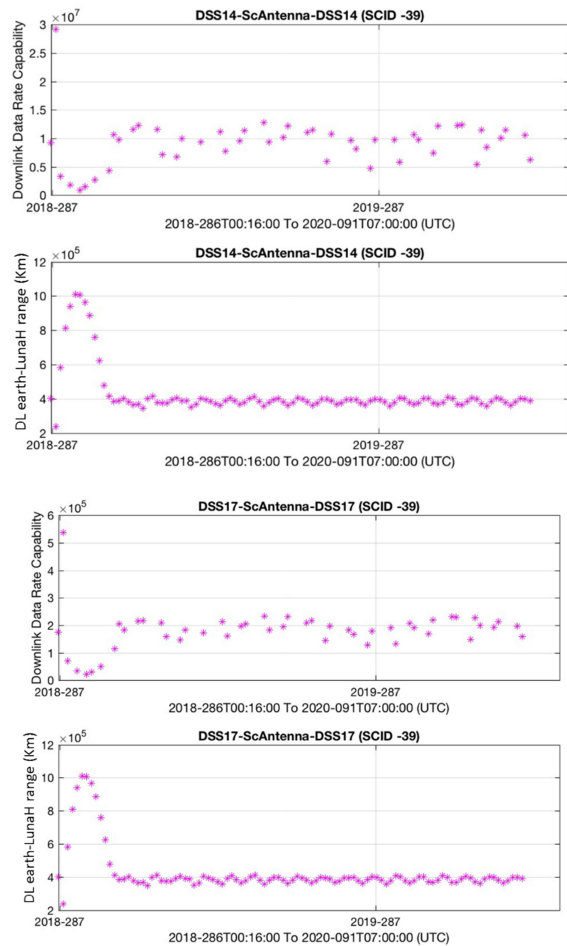

Figure 9.

Left) Data Rate capabilities and range for LunaH-Map mission when using DSN antennas. Right) Data Rate capabilities and range for LunaH-Map mission when using the 21-m antenna at Morehead State University. The vertical axes show downlink data rate capability in b/s (top plots) and Earth-to-spacecraft-range in Km (bottom plots). The horizontal axis is time in UTC assuming the original launch date of calendar day 286 in year 2018. These plots and analysis will need to be repeated with the final trajectory but they are presented here to show general telecommunication capabilities for the spacecraft across the mission life time.

In terms of ground support, LunaH-Map will use the services of the deep space network (DSN) and in particular the 34-m antennas at Goldstone, Canberra, Madrid, and the new 21-m antenna at Morehead State University (Cheung, K.M. 2015) which is now DSS number 17 and part of the NASA DSN complex. Link and coverage analysis has been performed to assess the data rate capabilities at different points of the mission. The data rate capabilities and range variation for the duration of the LunaH-Map mission (assuming a 2018 launch date and 18 months total duration) when using DSN and when using the 21-m antenna at Morehead State University are shown in Figure 9.

The telecommunication link margins are all sized to guarantee a margin of 3 dB in each of the different

Table 1.

Downlink Time Margin Across Different Mission Phases and for Different Values of Data Rate							
	Total DL Data (Mb)	HI DL Rate Dur (hrs)	Time margin for high data rate (hrs) assuming an 8 hr pass	Int DL Rate Dur (hrs)	Time margin for intermediate data rate (hrs) assuming an 8 hr pass	Low DL Rate Dur (hrs)	Time margin for low data rate (hrs) assuming an 8 hr pass
Launch & LEO	117.3	0.27	7.73	1.07	6.93	4.27	3.73
Cruise/Transition	703.9	1.60	6.40	6.41	1.59	25.63	-17.63
Science	234.6	0.53	7.47	2.14	5.86	8.54	-0.54

operational configurations: launch, cruise, lunar transition, and science. In terms of time margin during downlink, an analysis was performed to estimate the data volume between passes. It was found to be variable across the different mission phases, due to the frequency with which the passes will be taken. Specifically, during the launch phase, an estimate of 2 passes per day will generate a total estimated data volume per pass of 117 Mb. During the cruise phase, when the spacecraft is expected to downlink every 3 days, data volume per pass will be 703 Mb. During the science phase, where the expected passes are 1 per day, the data volume will be 234 Mb. Considering that the Iris radio has the capability for different data rates, an analysis was performed considering the highest LunaH-Map data rate (128 Kbps), an intermediate data rate (32 Kbps) and a low data rate (8 Kbps). The safe mode data rate of 62.5 bps was not considered given that if the system defaults to safe mode, only key telemetry points will be downlinked with the purpose of quickly troubleshoot the emergency and bring back the spacecraft into a nominal mode. Table 1 shows the time margin for each of the different phases and for the three data rates considered. It can be seen that the high data rate guarantees margin in all the situations, while the limited margin is available for intermediate data rates. The low data rate presents negative margins: this is expected given the high volume of data. However, if the

spacecraft was ever in a situation to be able to use only the low data rates, a reduction in the amount of data to transmit would have to be performed.

PROPULSION

LunaH-Map is equipped with an electric propulsion system for orbit transfer and station keeping. Developed by Busek Co. Inc., the BIT-3 (Busek Ion Thruster – 3 cm grid) propulsion system uses solid-storable iodine as a propellant [38], [39]. Iodine can be stored as a dense solid (4.9 g/cc), and its torr-level storage and operating vapor pressure are safe to launch and allows tank designs to be lightweight and conformal. The BIT-3 ion thruster and its complementary cathode neutralizer have demonstrated firing on iodine propellant (Figure 10), and performance has been verified on the ground via direct thrust measurement. During operation, the propellant tank is heated to produce iodine vapor, which is then fed to the BIT-3 thruster and the cathode neutralizer. The feed lines and flow control valves are heated slightly above the tank temperature in order to prevent condensation. The vapor flow rate is controlled by the tank heater, with closed-loop feedback from multiple temperature sensors on the tank. Thrust commanding is
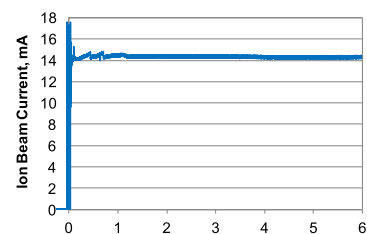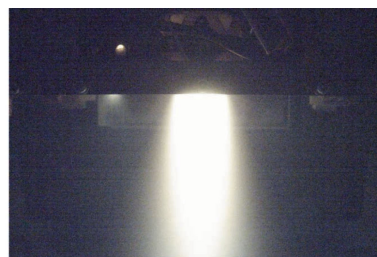

Figure 10.
Fully integrated BIT-3 iodine ion propulsion system (left) and demonstration of continuous, steady-state firing at nominal 70-W input power (middle and right).
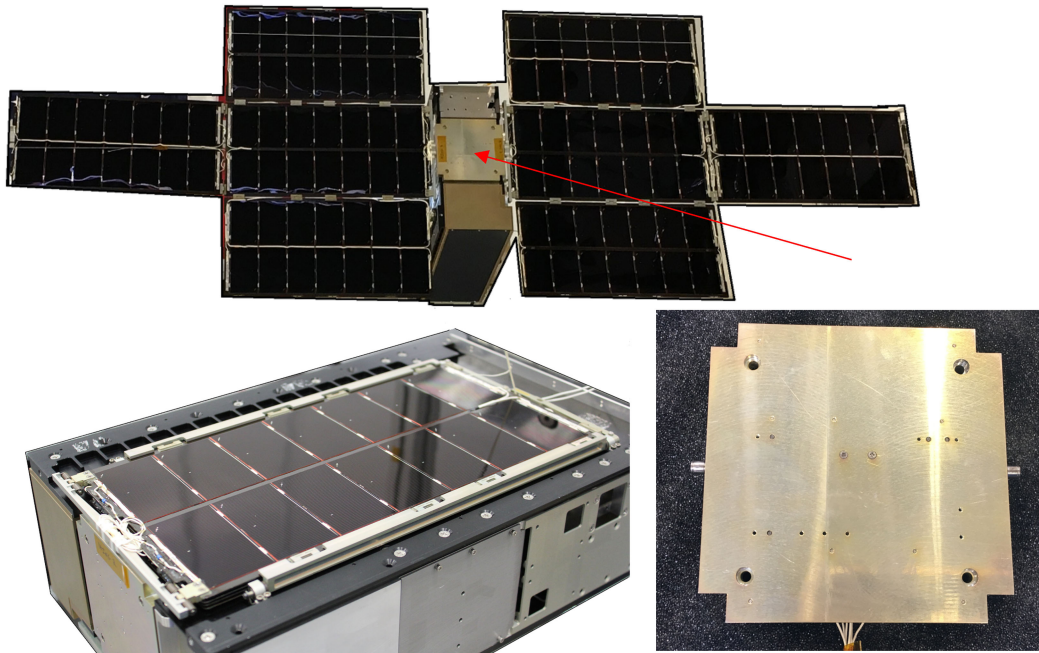
Figure 11.
MMA design LunaH-map solar array. Existing 3-panel wing design (top). Wing and launch restraint scaled for stowed requirements (bottom left). Also showing solar array drive assembly (bottom right).

close-loop controlled by the measured ion beam current and RF discharge power.

Figure 10 shows the BIT-3 flight system layout and packaging. The system's physical envelope is $180 \times 88 \times 102$ mm ($\sim$1.6U) and weighs 2.9 kg wet /1.4 kg dry. Other notable subsystem components include a 1.5-kg capacity iodine storage tank, a 2-axis gimbal, a miniaturized and $\sim$90% efficient Power Processing Unit (PPU), and a commercial-of-the-shelf iodine-compatible control valve. The gimbal utilizes two flight-grade stepper motors and is capable of $\pm10^{\circ}$ rotation in 0.1° resolution. The gimbal enables the single primary thruster to de-saturate the Reaction Wheel Assembly while in deep space. It can also counteract any shift in the center of gravity during flight.

The expected performance of the iodine BIT-3 system is based on actual thrust and specific impulse (Isp) data measured with iodine propellant, with some estimation of system heater power on-orbit. The flight BIT-3 system will be throttleable between 55 and 80W at the PPU input. The expected thrust and Isp within this power range are 0.64–1.23 mN and 1160–2220 s, respectively. When given sufficient power, the iodine BIT-3 system can provide a 6U/14 kg CubeSat a ΔV capability of 2.5 km/s. Note that another Artemis-1 CubeSat, Lunar IceCube, will also be using BIT-3 as a primary propulsion system.

POWER

MMA Design's HaWK^{TM} (High Watts per Kilogram) and eHaWK (Enhanced High Watts Per Kilogram) solar array technology leverages high TRL-8 MMA HaWK design components to produce an estimated 96 watt at beginning of life. MMA's solution can be stowed efficiently in a $2U \times 3U \times 10$ mm volume (see Figure 11). The LunaH-Map eHaWK^{TM} incorporates XTJ prime cells manufactured by Spectrolab, Inc. These cells have an average efficiency of 30.7%, with an active area of 27.22 cm^2. Spectrolab measures the electrical performance of each coverglass connected cell (CIC) using a steady-state solar simulator and these data are used by MMA Design to design each string assembly and provide similar performance across all strings. The LunaH-Map eHaWK^{TM} integrates a discrete bypass diode at the CIC level for reverse bias protection. Each string of 7 cells in series also includes a single blocking diode for string protection.

The LunaH-Map eHaWK^{TM} incorporates MMA's patented CubeSat Solar Array Drive Assembly (SADA, see Figure 11). This facilitates higher average orbital power and enables peak power tracking. The SADA features +/-180-degrees of actuation, up to 16 signal/power feedthrough conductors per wing, and actuation speeds up to 0.188 revolutions per minute.

AVIONICS, CONTROL, COMMAND, AND DATA HANDLING

Blue Canyon Technologies is providing the spacecraft avionics for the LunaH-Map mission. The BCT provided avionics include the LunaH-Map Guidance, Navigation, &
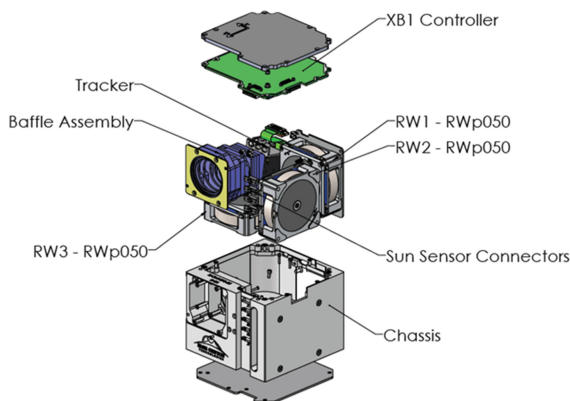
Figure 12.
Exploded view of BCT XB1-50 avionics module for LunaH-map.

Control (GN&C) Subsystem, the Command & Data Handling (C&DH) Subsystem, and the Electrical Power Subsystem. BCT is utilizing the heritage XB1-50 avionics suite to provide the GN&C and C&DH subsystems with a heritage Power Subsystem including a battery and power switching board. The LunaH-Map XB1-50 avionics include flexible interfaces, precise 3-axis attitude

determination & control provided by a BCT-designed star tracker, low jitter BCT Reaction Wheels, torque rods, and integrated control algorithms. The attitude control system enables precise orbit propagation of multiple objects enabling pointing with the Inertial, Earth or Lunar Reference frames. The XB1-50 enables bus functionality for GN&C, Electrical Power System (EPS), Thermal, C&DH, RF Communication, Data Storage and Flight Software, and control of the LunaH-Map propulsion system and solar array drive assembly. In addition, the system enables autonomous fault protection with the unique capability to recover from a spacecraft processor reset and autonomously resume a critical spacecraft burn and utilizes Deep Space Algorithm heritage obtained from the successful MarCO spacecraft.

Figure 12 illustrates the highly integrated XB1-50 Avionics Module for the LunaH-Map mission. This module provides the entirety of the GN&C and the C&DH subsystems. Three reaction wheels (each providing 50 mN-ms of momentum storage), the spacecraft processor, and the star tracker (including baffle) are integrated into the 10 cm × 10 cm × 13 cm module. Table 2 presents a summary of the LunaH-Map XB1-50 avionics capability.

Table 2.

XB1-50 LunaH-Map Avionics Performance		
	Parameter	**Performance**
General	Mass / Volume for Avionics	1.5 kg / 10 × 10 × 13 cm
	Nominal Power	XB1-50 < 6.8W
	Orbit Altitude / Orbit Lifetime	Deep Space & Lunar / 3 years
GN&C	Pointing Accuracy	±0.016° (1-sigma), 3 axes, 1 Trackers
	Pointing Stability	1 arc-sec/ 1-sec
	Maneuver rate	12 deg/sec
	Orbit Determination	Chebyshev Polynomial, SGP4, J2
CDH	Data Interfaces	Serial: LVDS, UART or SPI available
	Onboard Data Processing	Configurable via user loadable software
	Telemetry Acquisition	6 12bit Analog, 6 discrete inputs
	Commands	Real-time, stored, macro
	Onboard Data Storage	Redundant 8 Gbyte SD Cards (cold spare)
EPS	System Bus Voltage	5V, 12V and 28V bus supplies
	Energy Storage	9-Cell (3s3p) Li-Ion Battery with High and Low Side Inhibits
Misc.	SADA Interface	Avionics Autonomously Drive SADA to Optimize Power
	Propulsion	Utilize LunaH-Map's Busek BIT-3 propulsion system to provide linear Delta-V as well as autonomous momentum management

AUTONOMOUS OPERATIONS

The BCT LunaH-Map XB1-50 avionics suite is designed to make largely autonomous operations possible within a safe and flexible software framework. Some of this is accomplished within the fundamental software algorithms. For instance, in safe mode, the system is fully designed to autonomously find the Sun and maintain a safe attitude with power on the solar arrays, using a minimal set of sensor hardware. While the ground can involve itself in these activities as desired, for instance, to command a different momentum bias, such involvement is not necessary.

Autonomy is further enhanced by the system's conditional commanding capability, in which software commands (and "macros" consisting of timed command sequences) can be autonomously executed in response to predefined conditions. Both the conditions and the associated commands are table configurable, in both RAM and nonvolatile memory. An example of an autonomy rule on LunaH-Map is the continual monitoring of system momentum and, in the event of a high momentum, an autonomous start-up and actuation of the propulsion system. Additionally, LunaH-Map has a unique capability to store spacecraft commanded state information into nonvolatile memory during a thruster firing and, when enabled, to reload the spacecraft state autonomously in response to a processor reset and a resumption of mission critical thruster firings. The autonomy software is configurable and any flight software value can be used in autonomous command conditions.

XB1-50 SUBSYSTEMS

XB1-50 GUIDANCE, NAVIGATION, & CONTROL

The XB1-50 GN&C features 3-axis Stellar Attitude Determination in a micro-package. Built-in flexible commanding allows for multiple pointing reference frames: Inertial, LVLH, Earth-Fixed, Solar, Lunar. Precise 3-axis control is provided by low jitter reaction wheels providing 50 mNms of momentum storage along with integrated control algorithms. The software supports closed-loop simulation during system integration and test providing a test-like-you-fly environment. Interfaces to the LunaH-Map propulsion subsystem are accommodated and propulsion software drivers with LEO and Deep Space flight heritage are utilized.

XB1-50 Command & Data Handling System

XB1-50 provides autonomous operation and flexible command modes to support the required LunaH-Map mission modes. The software supports precision orbit propagation of multiple target objects via classical propagators as well as Chebyshev Polynomials. XB1-50 also incorporates radiation mitigation techniques such as maintaining a cold spare SD Card and utilizing a radiation-hardened watchdog timer to monitor processor upsets.

XB1-50 ELECTRICAL POWER SYSTEM

The LunaH-Map XB1-50 EPS board provides spacecraft electrical power control and distribution. Functionality includes solar array input power, battery interfaces, charge control, power regulation and distribution, and data acquisition. The EPS board functions as a peripheral to the XB1-50 controller board, such that telemetry from the EPS board is provided to the controller board, and commands are provided by the controller board to the EPS board to configure and control the EPS and spacecraft heaters. Custom power interfaces are located on the mission-specific LunaH-Map Expansion Power Board that interfaces to both the Main Power Board and the XB1-50 Controller Board.

XB1-50 RF COMMUNICATIONS

The LunaH-Map XB1-50 avionics communicate with JPL's Iris Deep Space Transponder.

OPERATIONS

Mission operations for the LunaH-Map program, including spacecraft command and control, telemetry processing and analysis, science data retrieval, archiving and product generation, and mission planning and scheduling, is performed on-campus at ASU in partnership with KinetX and Qwaltec. ASU's Mission Operations Center (MOC) is a multimission facility that will also house operations for components of the Mars 2020 rover and Psyche asteroid missions. For downlink operations, telemetry from the spacecraft is transmitted over X-Band via the Iris transponder and received by the DSN. The DSN forward the telemetry to ASU over a VPN connection where it is processed by the JPL-developed AMMOS Instrument Toolkit (AIT) Ground Data System. Throughout each satellite contact, real-time data from the spacecraft is downlinked for graphical trending and analysis for the state of health monitoring purposes. Additional stored flight software and spacecraft state of health telemetry are available for immediate analysis by the engineering and science teams. Following the satellite contact, custom data products are generated for the science, engineering, and KinetX mission planning teams. KinetX receives attitude prediction and history files, as well as thruster firing

history and a predicted events file; these are used to generate spacecraft ephemeris reconstruction and prediction files, navigation tracking requests, maneuver interface files, and light time files, which are all incorporated into the mission operations planning cycle. Similarly, the engineering and science teams use their data products to generate calibration or instrument requests to submit to the planning cycle, as necessary. In mid-2019, the LunaH-Map team successfully sent spacecraft commands from the ASU MOC through the DSN to the LunaH-Map flight Iris radio and the LunaH-Map C&DH. At the same test, the LunaH-Map Iris radio was characterized in a variety of power and bandwidth configurations, across a large swath of spectral parameters.

For uplink operations, the mission operations team uses a suite of custom Python tools to process all scheduling requests into a preliminary schedule. The schedule is verified against flight rules and resource/limit checks to ensure the spacecraft is safely able to complete all requested operations, at which point the necessary command sequences are generated and validated in AIT. The command format generated by AIT is a Communications Link Transmission Unit (CLTU) which is sent to the DSN and transmitted to LunaH-Map via the Space Link Extension—Forward CLTU Service at the next scheduled satellite contact. While time-critical anomaly resolution operations may require real-time/immediate commanding, the spacecraft will nominally operate via stored command sequences and onboard event checks.

Throughout the bulk of the mission (the cruise and transition phases), satellite contacts will only occur every few days. Operations will be highly automated during this period, relying heavily on limits monitoring and set point calibration do determine LunaH-Map's true nominal state of health across all subsystems. Anomaly resolution will be a joint undertaking between the science, engineering, and navigation teams to ensure the spacecraft stays on course throughout the mission. During the Science Phase, the operations tempo will ramp up into a daily cycle of tasks, including telemetry trending and analysis, data product generation and delivery, and mission planning. This will require seamless coordination between all mission teams and will result in frequent navigation solutions and knowledge/maneuver updates to the spacecraft. Several mission and flight readiness exercises, as well as full mission rehearsals between the ASU MOC and KinetX are planned prior to the first contact with the spacecraft to ensure the team and ground data systems are ready for flight. Finally, when the Science Phase has run its course, the last mission planning cycle will include a maneuver interface file from KinetX commanding a burn that will terminally degrade LunaH-Map's orbit into a crash at the lunar South Pole.

SUMMARY

LunaH-Map is a 6U spacecraft mission currently planned for launch in late 2020 or early 2021 on NASA's SLS Artemis-1. LunaH-Map will deploy from Artemis-1 and use a low-thrust propulsion system to maneuver into lunar orbit. The spacecraft will then maneuver into an elliptical, low-altitude perseline orbit that will enable the mission to spatially isolate and constrain the hydrogen enrichments within PSRs using a miniature neutron spectrometer. LunaH-Map will use a solid iodine ion propulsion system, X-Band radio communications through the NASA DSN, star tracker, C&DH and EPS systems from Blue Canyon Technologies, solar arrays from MMA Designs, LLC, mission design, and navigation by KinetX. Spacecraft systems design, integration, qualification, test, and mission operations are performed by ASU, AZ Space Technologies, and Qwaltec. LunaH-Map is currently on schedule for delivery of the spacecraft in early-to-mid 2020.

REFERENCES

[1] J. R. Arnold, "Ice in the lunar polar regions," *J. Geophys. Res.* vol. 84, pp. 5659–5668, 1979.

[2] A. Babuscia, C. Hardgrove, K.-M. Cheung, P. Scowen, and J. Crowell, "Telecommunications system design for interplanetary CubeSat mission: LunaH-Map," in *Proc. IEEE Aer. Conf.*, 2017, pp. 1–9.

[3] K. M. Cheung et al., "Next-generation ground network architecture for communications and tracking of interplanetary smallsats," in *Proc. CubeSat Workshop*, Calpoly, San Luis Obispo, 2015.

[4] R. N. Clark, "Detection of adsorbed water and hydroxyl on the moon," *Science*, vol. 326, pp. 562–564, 2009. doi: 10.1126/science.1178105.

[5] A. Colaprete et al., "Detection of water in the LCROSS ejecta plume," *Science*, vol. 330, pp. 463–468, 2010. doi:10.1126/science.1186986

[6] D. H. Crider and R. R. Vondrak, "The solar wind as a possible source of lunar polar hydrogen deposits," *JGR-Planets*, vol. 105, pp. 26773–26782, 2000. doi: 10.1029/2000JE001277.

[7] D. H. Crider and R. R. Vondrak, "Hydrogen migration to the lunar poles by solar wind bombardment of the moon," *Adv. Space Res.*, vol. 30, no. 8, pp. 1869–1874, 2002.

[8] C. Duncan, "Iris for INSPIRE CubeSat compatible, DSN compatible transponder," in *Proc. 27th Annu. AIAA/USU Small Satellite Conf.*, 2013, pp. 1–10.

[9] C. D'uston et al., "The mars odyssey gamma-ray spectrometer instrument suite," *Space Sci. Rev.*, vol. 110, pp. 37–83, 2004.

[10] R. C. Elphic, V. R. Eke, L. F. A. Teodoro, D. J. Lawrence, and D. B. J. Bussey, "Models of the distribution and abundance of hydrogen at the lunar south pole," *Geophys. Res. Lett.*, vol. 34, pp. 1–5, 2007.

[11] V. R. Eke, L. F. A. Teodoro, and R. C. Elphic, "The spatial distribution of polar hydrogen deposits on the Moon," *Icarus*, vol. 200, pp. 12–18, 2009. doi:10.1016/j.icarus.2008.10.013

[12] W. C. Feldman, S. Maurice, A. B. Binder, B. L. Barraclough, R. C. Elphic, and D. J. Lawrence, "Fluxes of fast and epithermal neutrons from lunar prospector: Evidence for water ice at the lunar poles, *Science*, vol. 281, pp. 1496–1500, 1998. doi: 10.1126/science.281.5382.1496.

[13] W. C. Feldman et al., "Gamma-ray, neutron, and alpha-particle spectrometers for the lunar prospector mission," *J. Geophys. Res.*, vol. 109, 2004, Art. no. E07S06. doi: 10.1029/2003JE002207.

[14] E. A. Fisher et al., "Evidence for surface water ice in the lunar polar regions using reflectance mea- surements from the lunar orbiter laser altimeter and temperature measurements from the diviner lunar radiometer experiment," *Icarus*, vol. 292, pp. 74–85, 2017.

[15] A. Genova and D. Dunham, "Trajectory design for the lunar polar hydrogen mapper mission," in *Proc. 27th AAS/AIAA Space Flight Mech. Meeting*, Feb. 5–9, 2017, pp. 1–15.

[16] J. Glodo, "Scintillation Properties of 1 Inch Cs2LiYCl6: Ce Crystals," *IEEE Trans. Nucl. Sci.*, vol. 55, no. 3, pp. 1206–1209, Jun. 2008.

[17] J. O. Goldsten et al., "The MESSENGER gamma-ray and neutron spectrometer," *Space Sci. Rev.*, vol. 131, pp. 339–391, 2007. doi: 10.1007/s11214-007-9262-7.

[18] P. O. Hayne et al., "Evidence for exposed water ice in the Moon's south polar regions from Lunar Reconnaissance Orbiter ultraviolet albedo and temperature measurements," *Icarus*, vol. 255, pp. 58–59, 2015.

[19] E. B. Johnson et al., "Development of the LunaH-Map miniature neutron spectrometer," *Proc. SPIE*, vol. 10392, pp. 1–10, 2017.

[20] D. J. Lawrence, R. C. Elphic, W. C. Feldman, H. O. Funsten, T. H. Prettyman, "Performance of orbital neutron instruments for spatially resolved hydrogen measurements of airless planetary bodies," *Astrobiology*, vol. 10, pp. 183–200, 2010. [Online]. Available: https://doi.org/10.1089/ast.2009.0401.

[21] D. J. Lawrence et al., "Evidence for water ice near mercury's North Pole from MESSENGER neutron spectrometer measurements," *Science*, vol. 339, pp. 292–297, 2012. doi: 10.1126/science.1229953.

[22] D. J. Lawrence, P. N. Peplowski, J. B. Plescia, B. T. Greenhagen, S. Maurice, and T. H. Prettyman, "Bulk hydrogen abundances in the lunar highlands: Measurements from orbital neutron data," *Icarus*, vol. 255, pp. 127–134, 2015.

[23] D. J. Lawrence, "A tale of two poles: Toward understanding the presence, distribution, and origin of volatiles at the polar regions of the Moon and Mercury," *J. Geophys. Res. Planets*, vol. 122, pp. 21–52, 2017. doi:10.1002/2016JE005167

[24] P. G. Lucey, The poles of the moon, *Elements*, vol. 5, no. 1, pp. 41–46, 2009.

[25] I. G. Mitrofanov et al., "Hydrogen mapping of the lunar south pole using the LRO neutron detector experiment LEND," *Science*, vol., 330, pp. 483–486, 2010. doi: 10.1126/science.1185696.

[26] I. G. Mitrofanov et al., "Lunar exploration neutron detector for the NASA lunar reconnaissance orbiter," *Space Sci. Rev.*, vol. 150, pp. 183–207, 2010. doi: 10.1007/s11214-009-9608-4.

[27] I. G. Mitrofanov et al., "Dynamic albedo of neutrons (DAN) experiment onboard NASA's mars science laboratory," *Space Sci. Rev.*, vol. 170, pp. 559–582, 2012. doi: 10.1007/s11214-012-9924-y.

[28] S. Nozette et al., "The clementine bistatic radar experiment," *Science*, vol. 274, pp. 1495–1498, 1996.

[29] C. M. Pieters, "Character and spatial distribution of OH/H2O on the surface of the moon seen by M3 on chandrayaan-1," *Science*, vol. 326, pp. 568–582, 2009. doi: 10.1126/science.1178658.

[30] C. M. Pieters and P. A. Englert, Eds., *Remote Geochemical Analysis; Elemental and Mineralogical Composition*. Cambridge, UK: Cambridge Univ. Press, 1993.

[31] T. H. Prettyman et al., "Dawn's gamma ray and neutron detector," *Space Sci. Rev.*, vol. 163, 371–459, 2011. doi: 10.1007/s11214-011-9862-0.

[32] T. H. Prettyman, "Remote sensing of chemical elements using nuclear spectroscopy," in T. Spohn, T. Johnson, and D. Breuer (Eds.), *Encyclopedia of the Solar System, (3rd Ed)*. New York, NY, USA: Elsevier, 2014, pp. 1161–1183.

[33] T. H. Prettyman, P. A. J. Englert, and N. Yamashita, "Fundamentals of X-ray, gamma-ray, and neutron spectroscopy," in J. L. Bishop, J. F. Bell III, and J. E. Moersch (Eds.), *Remote Compositional Analysis: Techniques for Understanding Spectroscopy, Mineralogy, and Geochemistry of Planetary Surfaces*. Cambridge, UK: Cambridge Univ. Press, 2019, ch. 9.

[34] L. Rubanenko, J. Venkatraman, and D. A. Paige, "Thick ice deposits in shallow simple craters on the moon and mercury," *Nature Geosci.*, vol. 12, pp. 597–601, 2019. doi: 10.1038/s41561-019-0405-8.

[35] M. A. Siegler et al., "Lunar true polar wander inferred from polar hydrogen," *Nature*, vol. 531, no. 7595, pp. 480–84, 2016.

[36] J. M. Sunshine et al., "Temporal and spatial variability of lunar hydration as observed by the deep impact spacecraft," *Science*, vol. 326, pp. 565–568, 2009. doi: 10.1126/science.1179788.

[37] L. F. A. Teodoro, V. R. Eke, R. C. Elphic, W. C. Feldman, and D. J. Lawrence, "How well do we know the polarhydrogen distribution on the Moon?," *J. Geophys. Res. Planets*, vol. 119, pp. 574–593, 2014. doi: 10.1002/2013JE004421.

[38] M. Tsay et al., "Neutralization demo and thrust stand measurement for BIT-3 RF ion thruster," in *Proc. AIAA Propul. Energy Forum*, 2017, Paper AIAA-2017-4890.

[39] M. Tsay et al., "Qualification model development of cubesat RF ion propulsion system BIT-3," in *Proc. 31st Int. Symp. Space Technol. Sci.*, 2017, Paper ISTS-2017-f-059.

[40] H. C. Urey, *The Planets: Their Origin and Development*. New Haven, CT, USA: Yale Univ. Press, 1952, pp. 17–18.

[41] K. Watson, B. Murray, and H. Brown, "On the possible presence of ice on the moon," *J. Geophys. Res.*, vol. 66, pp. 1598–1600, 1961. doi: 10.1029/JZ066i005p01598.

[42] W. V. Boynton et al., "The Mars Odyssey Gamma-Ray Spectrometer Instrument Suite," *Space Science Reviews* 110, pp. 37–83, 2004.